Peer-reviewed version available at *Nanomaterials* **2020**, *10*, 711; doi:10.3390/nano10040711

Tunable photodetectors via *in situ* thermal conversion of TiS_3 to TiO_2

Foad Ghasemi[1,2,+], Riccardo Frisenda*[3,+], Eduardo Flores[4], Nikos Papadopoulos[5], Robert Biele[6,7], David Perez de Lara[1], Herre van der Zant[5], Kenji Watanabe[8], Takashi Taniguchi[8], Roberto D'Agosta[6,9], Jose R. Ares[4], Carlos Sánchez[4,10], Isabel J. Ferrer[4,10] and Andres Castellanos-Gomez*[3]

[1] Instituto Madrileño de Estudios Avanzados en Nanociencia (IMDEA-Nanociencia), Campus de Cantoblanco, E-28049 Madrid, Spain.

[2] Nanoscale Physics Device Lab (NPDL), Department of Physics, University of Kurdistan, 66177-15175 Sanandaj, Iran.

[3] Materials Science Factory, Instituto de Ciencia de Materiales de Madrid (ICMM-CSIC), E-28049, Madrid, Spain.

[4] Materials of Interest in Renewable Energies Group (MIRE Group), Dpto. de Física de Materiales, Universidad Autónoma de Madrid, UAM, Campus de Cantoblanco, E-28049 Madrid, Spain.

[5] Kavli Institute of Nanoscience, Delft University of Technology, Lorentzweg 1, Delft 2628 CJ, The Netherlands.

[6] Nano-Bio Spectroscopy Group and European Theoretical Spectroscopy Facility (ETSF), Universidad del País Vasco CFM CSIC-UPV/EHU-MPC & DIPC, Av.Tolosa 72 ,20018, San Sebastián, Spain.

[7] Institute for Materials Science and Max Bergmann Center of Biomaterials, TU Dresden, 01062 Dresden, Germany.

[8] National Institute for Materials Science, Namiki 1-1, Tsukuba, Ibaraki 305-0044, Japan.

[9] IKERBASQUE, Basque Foundation for Science, 48013 Bilbao, Spain.

[10] Instituto Nicolás Cabrera, Universidad Autónoma de Madrid, UAM, Campus de Cantoblanco, E-28049 Madrid, Spain.

*E-mail: riccardo.frisenda@csic.es, andres.castellanos@csic.es.

[+] These two authors contributed equally to this work.

Abstract: In two-dimensional materials research, oxidation is usually considered as a common source for the degradation of electronic and optoelectronic devices or even device failure. However, in some cases a controlled oxidation can open the possibility to widely tune the band structure of 2D materials. In particular,

We demonstrate the controlled oxidation of titanium trisulfide (TiS_3), a layered semiconductor that attracted much attention recently thanks to its quasi-1D electronic and optoelectronic properties and its direct bandgap of 1.1 eV. Heating TiS_3 in air above 300 °C gradually converts it into TiO_2, a semiconductor with a wide bandgap of 3.2 eV with applications in photo-electrochemistry and catalysis. In this work, we investigate the controlled thermal oxidation of individual TiS_3 nanoribbons and its influence on the optoelectronic properties of TiS_3-based photodetectors. We observe a step-wise change in the cut-off wavelength from its pristine value ~1000 nm to 450 nm after subjecting the TiS_3 devices to subsequent thermal treatment cycles. Ab-initio and many-body calculations confirm an increase of the bandgap of titanium oxysulfide ($TiO_{2-x}S_x$) when increasing the amount of oxygen and reducing the amount of sulfur.

Keywords

2D materials, photodetectors, oxidation, TiS_3, TiO_2, Raman spectroscopy, DFT GW.

Introduction

Low-dimensional semiconductors are attracting increasing interest in the scientific community working on optoelectronic devices thanks to outstanding optical and electronic properties combined with reduced dimensionality [1-3]. The large surface-to-volume ratio of two-dimensional (2D) materials benefits many applications such as gas-sensing, but it may enhance the sensitivity of these materials to oxidation compared to bulk materials. Moreover, lattice vacancies and atomic-level defect combined with the presence of light can accelerate the oxidation process [4-8], which is typically accompanied by a degradation of the electrical and optical properties reducing the device performance [9-10]. Furthermore, shining high intensity light on 2D materials can induce additional processes of photooxidation [11-14]. The overall performance reduction induced by oxidation seems one of the main issues to solve in developing industrial applications based on 2D materials, therefore controlling the oxidation process is a very active subject for both fundamental and applied research in the context of band engineering.

Main text

Titanium trisulfide (TiS_3) is a layered semiconductor which has attracted much attention recently thanks to its quasi-1D electronic and optoelectronic properties [15-18] and its direct bandgap of 1.1 eV [19-25]. Using first-principles calculations, Iyikanat *et al.* showed that TiS_3 can react with various forms of oxygen [26]. An experimental demonstration was given by Molina-Mendoza *et al.,* who reported thermogravimetric analysis (TGA) of bulk TiS_3 in oxygen atmosphere showing the partial conversion of the material into TiO_2, a large bandgap (3.2 eV) insulator with a wide range of applications [19, 27-29]. In this article we investigate the controlled thermal oxidation of individual TiS_3 nanoribbons and its influence on the optoelectronic properties of TiS_3-based photodetectors. We first study the oxidation of TiS_3 powder and single nanoribbons deposited on a glass substrate. Using Raman spectroscopy and optical analysis we can monitor the material properties as a function of time while

heating at 320 °C in air. We find that an individual TiS_3 nanoribbon converts to crystalline TiO_2 in approximately 10 minutes. Control experiments performed on TiS_3 nanoribbons fully encapsulated between hexagonal boron nitride flakes confirm that the direct contact between TiS_3 and air is necessary for the oxidation process to happen. After establishing the change in material properties we demonstrate the controlled oxidation of a TiS_3 nanoribbon photodetector that allows tuning the cut-off wavelength and sensitivity of the device. By monitoring the change in its current-voltage characteristics and in its spectral photoresponse, we find that in the pristine state the cut-off wavelength is above 650 nm (≈1100 nm according to previous works [19]) and that upon oxidation a blue-shift happens reaching a cut-off wavelength of 450 nm. Various intermediate states are observed, demonstrating the tunability of the nanoribbon bandgap. Ab-initio and many-body calculations confirm an increase of the bandgap near to that of titanium oxysulfide ($TiO_{2-x}S_x$) when increasing the amount of oxygen and reducing the amount of sulfur.

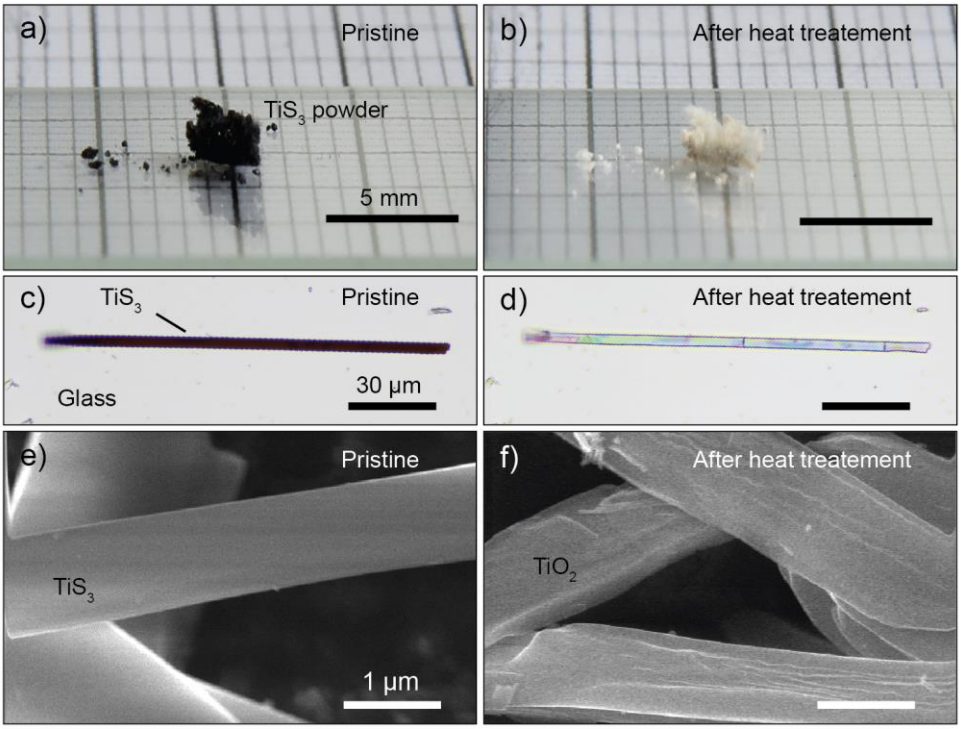

Figure 1: a) Photograph of TiS_3 powder onto a glass slide. b) Photograph of the same powder of panel (a) after heating in air for 5 minutes at 350 °C. c) Optical image of an individual TiS_3 nanoribbon transferred onto a glass substrate, recorded in transmission illumination mode under the microscope. d) Same as (c) after heating in air for 5 minutes at 350 °C. e-f) FEGSEM image of pristine TiS_3 (e) and after heating at 400 °C in air (f). Note that the images in panel (e) and (f) correspond to different nanoribbons.

The starting TiS_3 material was synthetized by a solid-gas reaction using Ti powder and sulfur powder sealed into a quartz ampoule and kept at 550 °C for 20 hours. Additional details about the syn-

thesis and elemental characterization of TiS3 can be found in Refs. [ ]. Figure 1a shows an optical picture of TiS_3 powder while Figure 1b shows the same powder after heating it for 5 minutes at 350 °C in air. After heating the material we observe a dramatic change of its appearance, with a clear color from black to white, due to the conversion of TiS_3 to TiO_2. Thanks to the layered structure of TiS_3, individual nanoribbons can be isolated by mechanical exfoliation. To study an individual TiS_3 nanoribbon, we first exfoliate the powder onto Nitto tape and then transfer part of the flakes from the tape to a viscoelastic polidimethylsiloxane (PDMS) stamp. After the identification we transfer the chosen nanoribbon to a different substrate (such as glass, SiO_2/Si…) with an all-dry deterministic transfer method [32-33].

A typical TiS_3 nanoribbon transferred onto a glass slide is shown in Figure 1c. The microscope picture is recorded in transmission mode and the nanoribbon appears black since it is absorbing most of the white light due to the bandgap of 1.1 eV. The nanoribbon has a length of approximately 150 μm (oriented along the crystal *b* axis) and a width of 5 μm (*a* axis). Figure 1d shows the same nanoribbon after heating it for 5 minutes at 350 °C in air. The morphology of the nanoribbon appears intact, but the substantial change in color indicates that its absorption, which is related to the bandgap and the band-structure, has changed dramatically. The change from black to white/transparent due to a reduction of the light absorption indicates an opening of the bandgap. A higher resolution picture of the initial and final status of TiS_3 nanoribbons can be obtained using electron microscopy. Figure 1e-f shows a field emission gun scanning electron microscopy (FEGSEM) image of TiS_3 nanoribbons before and after the heat treatment. As can be seen from the images, the nanoribbons morphology is maintained after the heat treatment, although the final nanoribbons show higher roughness.

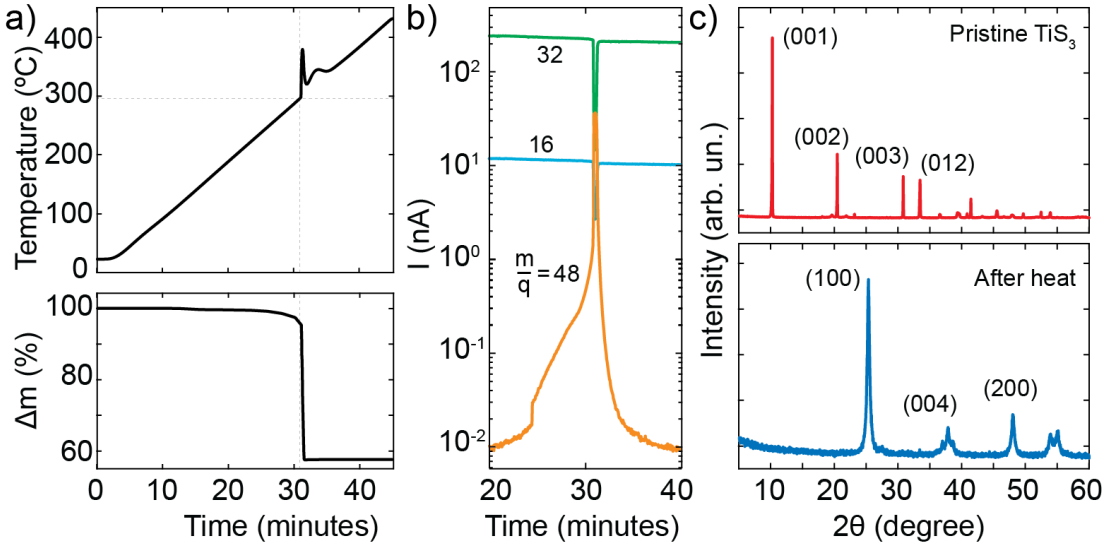

Figure 2: a) TGA curves of TiS_3 during the heating under a flux of air of 90 ml/min at 10 °C/min, time dependence of the temperature (top) and time evolution of the loss of mass (bottom). b) Ionic currents at different m/q ratios as a function of time during the TGA experiment. c) XRD patterns of TiS_3 before and after the heating treatment.

To gain deeper insight into the thermal oxidation process of TiS_3 we used TGA coupled to mass spectrometry (MS). Figure 2a shows a TGA curve of TiS_3 kept under a flux of 90 ml/min of air and heated at a rate of 10 °C/minute. The graph of temperature as a function of time, shown in the top panel of Fig. 2a, displays a discontinuity at approximately 30 minutes, indicative of an exothermic reaction occurring at 300 ± 10 °C. This reaction is accompanied by a loss of approximately 43% of the initial mass (see the bottom panel of Fig. 2a) that is consistent with the difference between the mass of TiS_3 and TiO_2 (44%). These results indicate that the conversion of TiS_3 into TiO_2 take place under atmospheric conditions starting at 300 °C. A more in-depth look can be achieved using a mass spectrometer to detect the species present during the reaction. Figure 2b shows the ionic currents at m/q = 16, 32 and 48 (m/q is the ration between the atomic mass m and the atomic charge q of the species) as a function of time recorded during the TGA experiment, corresponding to O_2 (whose cracking pattern shows two signals) and SO_2. The dip observed at 30 minutes in the traces of m/q = 16 and 32 indicates that the O_2 present in the atmosphere is reacting with TiS_3. At the same time, the peak in current of m/q = 48 is consistent with the liberation of sulfur atoms from TiS_3 and their successive reaction with oxygen to form gaseous SO_2.

The composition of the final product after the thermal treatment of TiS_3 is studied with x-ray diffraction measurements (XRD). The x-ray diffraction measurements were performed using a X-pert PRO diffractometer under a $\Theta/2\Theta$ configuration. Figure 2c shows XRD patterns of TiS_3 before and after the heating treatment with the main diffraction planes indicated. In the pristine material only a single polycrystalline phase is observed and the XRD peaks correspond to TiS_3. After the heating the XRD pattern changed significantly and the new peaks correspond to polycrystalline anatase TiO_2. Comparing the two spectra it can be seen that the diffraction peaks after the treatment are broader than the ones before, indicating that the produced TiO_2 has crystallites of smaller size. Overall the previous results support a scenario in which TiS_3 heated above 300 °C in ambient conditions undergoes the global exothermic reaction: $TiS_3 + 4O_2 \rightarrow TiO_2 + 3SO_2$, which converts the trisulfide in anatase TiO_2.

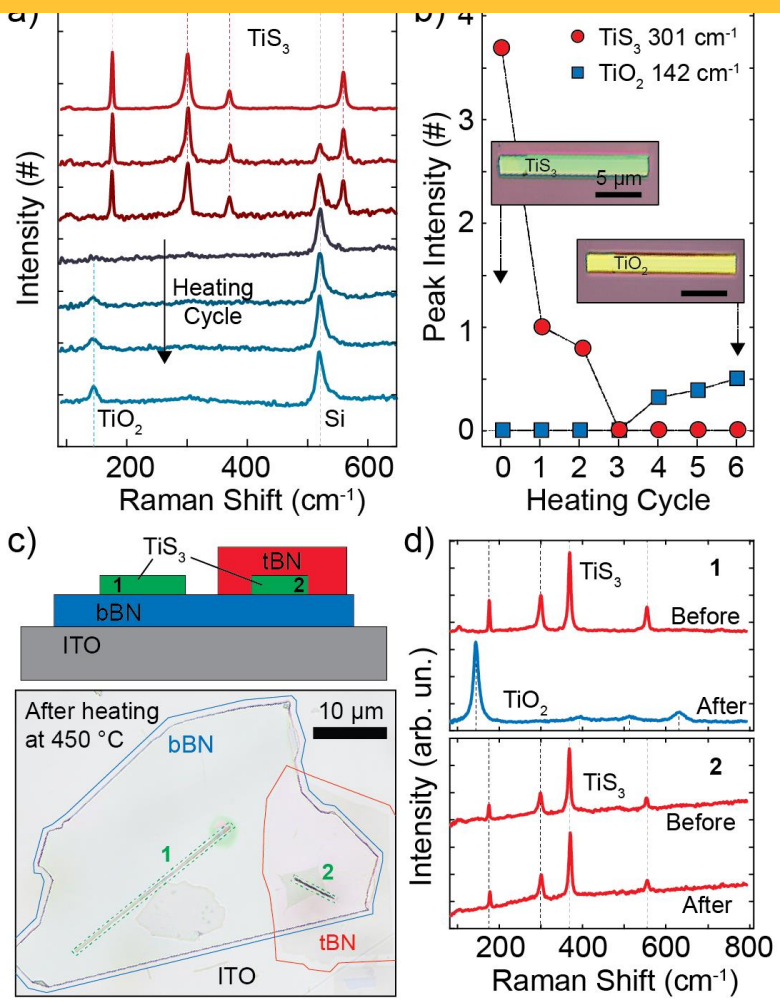

Figure 3: a) Raman spectra of a TiS_3 nanoribbon onto a SiO_2/Si substrate recorded in its pristine state (top) and during heating cycles at 320 °C. The spectra have been offset for clarity and each cycle corresponds to 2 minutes at 320 °C. b) Intensity of the peaks at 142 cm^{-1} and 301 cm^{-1} as a function of heating cycle. The inset shows an optical picture of the pristine TiS_3 nanoribbon onto SiO_2/Si (left) and of the same nanoribbon after heat treatment (right). c) Schematic of the boron-nitride/TiS_3 stack (top) where 1 is not encapsulated and 2 is fully encapsulated. Optical picture of the sample after heating it at 450 °C for 30 minutes (bottom). We highlighted the contour of two boron nitride flakes (in red and blue) and of the nanoribbons (green) for clarity. d) Raman spectra of the unencapsulated (**1**, top) and encapsulated (**2**, bottom) nanoribbons of panel (c) recorded before and after heating the sample.

After characterizing the thermal oxidation of bulk TiS_3, we focus on individual nanoribbons oxidation which is interesting for the fabrication of high-quality optoelectronic devices. We start by using Raman spectroscopy to study the composition of a single nanoribbon. Figure 3a shows the Raman spectra of a TiS_3 nanoribbon recorded in its pristine form (after deposition onto a SiO_2/Si substrate)

and during a heating cycle with spectra taken every 2 minutes while heating the sample at a temperature of 320 °C. The Raman spectra were recorded in a Raman Microscope (SENTERRA II, Bruker) while illuminating the sample with a laser of 532 nm focused in a circular spot (area ~2 μm^2, power 2 mW, power density 1 $mW/\mu m^2$) and integration time 20 s. The power density that we use is lower than the threshold density for photooxidation of the TiS_3, which we estimate to be 5 $mW/\mu m^2$ (see Section S4 of the Supporting Information). The Raman signal of the pristine TiS_3 shows four prominent peaks due to TiS_3 and a very weak peak at 520 cm^{-1} due to the silicon substrate. The peaks at energies 177 cm^{-1}, 302 cm^{-1}, 371 cm^{-1}, and 559 cm^{-1} correspond to A_g Raman modes of the TiS_3 nanoribbon and are in good agreement with the modes reported for bulk TiS_3 [34]. After heating up the sample we observe a reduction of the intensity of the TiS_3 peaks and an increase of the Si peak intensity during the first two cycles (4 minutes) that can be attributed to an increase of the transparency of the nanoribbon. After approximately 6 minutes of heating (after three cycles) we observe the quenching of the TiS_3 peaks with only the 520 cm^{-1} Si peak visible in the Raman spectrum of the sample. The spectra recorded after 8, 10 and 12 minutes of heating show the appearance of a new peak centered at 142 cm^{-1}. This peak is consistent with the signature of an E_g Raman mode of TiO_2 [35-36]. The evolution of the Raman spectra of the nanoribbon shows that a pristine TiS_3 nanoribbon can be converted to TiO_2 by heating at 320 °C. The TiS_3 to TiO_2 oxidation process can be readily visualized from the plot in Figure 3b in which we show the extracted intensities of the 142 cm^{-1} (TiO_2) and 302 cm^{-1} (TiS_3) peaks as a function of the number of heating cycle. Apart from the change in the Raman signal, we also observe a clear change in the color of the nanoribbon deposited on the SiO_2/Si surface from green to yellow during the conversion process as shown in the inset of Figure 3b.

To study the role of the environment on the oxidation process of a single nanoribbon we fabricated a hexagonal boron nitride (h-BN) encapsulated TiS_3 nanoribbon on top of a transparent indium tin oxide (ITO) substrate. The top panel of Figure 3c shows the schematic of the samples. We first transferred a flake of h-BN onto the ITO surface and then transferred two TiS_3 nanoribbons onto the h-BN surface. We finally transferred a second h-BN flake covering just one of the two TiS_3 nanoribbons. Figure 3c shows an optical picture of the fabricated stack after heating it. We recorded the Raman spectrum of each nanoribbon before and after heating up the sample at 450 °C (a temperature much larger than the threshold for oxidation of 300 °C). Figure 3d shows the Raman spectra of the two nanoribbons before heating that display very similar features and are both characterized by the four TiS_3 peaks discussed above. Notice that compared to Figure 3a the Si peak is missing since the substrate is ITO. When comparing the spectra after heating at 450 °C for 30 minutes we observe a large difference between the two nanoribbons. While the fully encapsulated nanoribbon (2) does not show a significant change of its spectrum, indicating that the final material is TiS_3, the unencapsulated flake (1) shows a dramatic change in its spectrum, due to the conversion from TiS_3 to TiO_2. The encapsulation (with bottom and top h-BN) prevents the oxidation of the TiS_3 nanoribbons from happening. The effect of the h-BN layers are visible also in the optical picture of Figure 3c where it can be seen a big difference in the aspect of the two nanoribbons (one being oxidized and the other not). As a side note, the Raman spectrum of the oxidized uncovered nanoribbon shows

Preprints (www.preprints.org) | NOT PEER-REVIEWED | Posted: 1 March 2020 doi:10.20944/preprints202003.0008.v1

Peer-reviewed version available at Nanomaterials 2020, 10, 711; doi:10.3390/nano10040711

These peaks, which are sensible to the TiO_2 crystalline phase, are due to anatase TiO_2 in agreement with the results from the XRD measurements of Figure 2c.

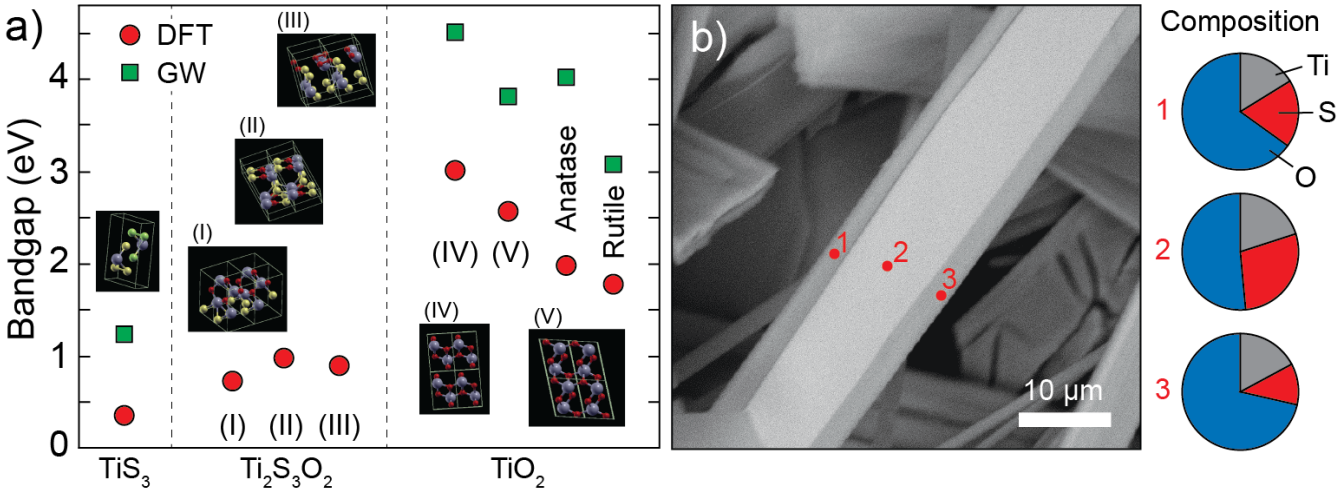

Figure 4: a) Bandgap calculated from DFT (red circles) and GW (green squares) for TiS_3, TiO_2 and intermediate phases composed of 50% TiS_3 and 50% of TiO_2 (indicated as $Ti_2S_3O_2$). b) FEGSEM image of a TiS_3 nanoribbon heated up to 300 °C during 1 hour. Spatially resolved electron diffraction measurements at the positions indicated by the red dots (right panel) reveal a higher oxygen concentration along the ribbon edges.

The experiments discussed above show that a thermal oxidation process can convert TiS_3 nanoribbons into TiO_2 and that this evolution can be followed on a single ribbon level with Raman spectroscopy. We now focus on the changes in the band-structure of the system when passing from TiS_3 to TiO_2. To calculate the electronic band structure, we have performed state-of-the-art ab-initio Density Functional Theory (DFT) calculations with a pseudo-potential plane-wave method as implemented in the PWSCF code of the Quantum-ESPRESSO suite [37-39]. Figure 4a shows the calculated bandgap of TiS_3 (left), intermediate $Ti_2S_3O_2$ phases (middle) and of four different polytypes of TiO_2 (right). The different materials are ordered along the horizontal axis according to the total energy (when going from left to right the total energy decreases and the thermodynamic stability increases). Because DFT typically underestimates the band gap energy [40], we have further performed a more refined calculation for some of the structures based on non-self-consistent GW method.

Both DFT and GW calculations predict that the bandgap energy increases monotonically when the content of sulfur decreases and the oxygen increases. The stable intermediate titanium oxysulfide phases predicted by the theory are consistent with FEGSEM measurements of partially oxidized nanoribbons. The left panel of Figure 4b shows a FEGSEM image of such a nanoribbon in which the core and the edges show different contrast. The EDX analysis of the image performed in the centre and at the edges of the nanoribbon reveals a higher oxygen concentration along the edges. This indicates that the oxidation process occurs through the formation of intermediate phases $TiO_{2-x}S_x$

Preprints (www.preprints.org) | NOT PEER-REVIEWED | Posted: 1 March 2020 doi:10.20944/preprints202003.0008.v1

Peer-reviewed version available at Nanomaterials 2020, 10, 711; doi:10.3390/nano10040711

scope pictures of partially oxidized nanoribbons in Fig. S2, Section S1 of the Supporting Information.

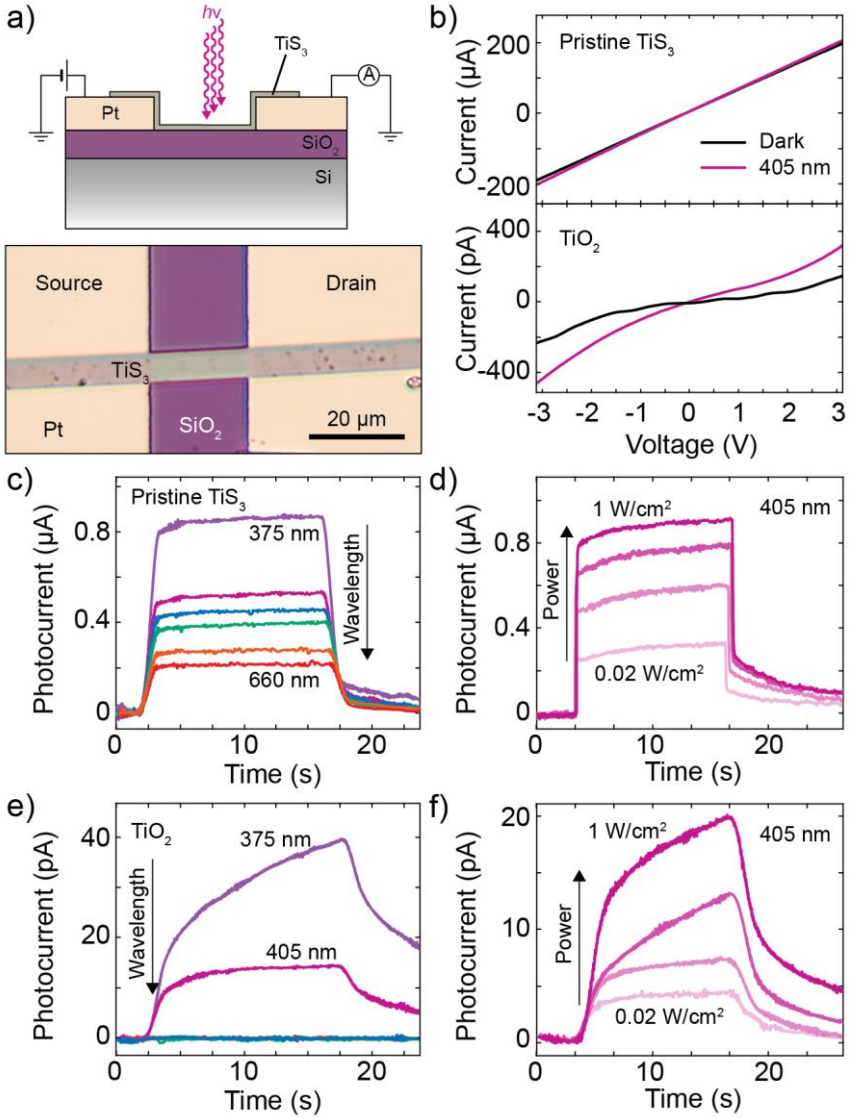

Figure 5: a) Schematic of a TiS_3 photodetector (top). Optical microscope image of a TiS_3 photodetector (bottom). b) Current-voltage characteristics of the sample in its pristine state (top) and after oxidation of the nanoribbon (bottom). The black line is the current recorded with the device kept in dark while the purple line is under illumination at 405 nm. (c-f) Photocurrent as a function of time recorded while modulating the intensity of the incident light with a square wave on the pristine TiS_3 photodetector (c-d) and on the TiO_2 (e-f). The colors in (c, e) correspond to different incident wavelengths (375 nm, 405 nm, 420 nm, 530 nm, 605 nm, 660 nm) while the shades of purple in (d, f) correspond to different incident power densities from 0.02 W/cm² to 1 W/cm² at a fixed wavelength of 405 nm.

After establishing the change in the optical appearance and vibrational properties of TiS_3 nanoribbons after high temperature treatment, due to the oxidation of TiS_3 to TiO_2, we now investigate electronic transport through an individual nanoribbon and monitor the change of the optoelectronic properties. We fabricate a TiS_3 photodetector by transferring an individual TiS_3 nanoribbon onto two pre-patterned platinum electrodes separated by a distance of 20 μm. Figure 5a shows a schematic of the device and an optical image of the pristine TiS_3 device. The TiS_3 nanoribbon bridges the two electrodes and light can be shined on the exposed TiS_3 channel to study its photoresponse. Figure 5b shows the current-voltage characteristics (*I*-*V*s) of the device recorded just after the fabrication (top panel) and after heating it for 12 minutes at 320 °C (bottom panel). Photographs of the device at various stages of the evolution are shown in Fig. S6, Section S3 of the Supporting Information. The *I*-*V*s where recorded in dark conditions (black curve) and under global illumination at 405 nm with power density 1 W/cm^2 (purple curve). Comparing the *I*-*V*s of the pristine with those of the oxidized device we can see a difference in the shape of both *I*-*V*s and in the magnitude of the current. The TiS_3 device is characterized by linear *I*-*V*s and current in the range of μA while the oxidized device has non-linear *I*-*V*s with currents in the pA (approximately six orders of magnitude lower than the pristine device). In both cases the device responds to light, evidenced by the larger current observed in the *I*-*V*s under illumination at 405 nm in comparison to the ones recorded in dark. Considering that the area of the channel is 100 μm^2 and that the incident optical power is 1 W/cm^2, the responsivity of the device to 405 nm at 3 V (-3 V) is 8 A/W (11 A/W) in the pristine (TiS_3) case and 0.00016 A/W (0.00022 A/W) in the oxidized case. In total in this work we fabricated and characterized 11 devices that have been heated at 320 °C in air, see Section S3 of the Supporting Information. In 4 cases out of 11 we observed the conversion of the TiS_3 photodetector in a TiO_2 one without losing the functionality (success rate 36%).

In order to study the responsivity of the device to different wavelengths and incident optical powers we measure current-time traces while modulating in time the intensity of the incident light with a square wave. Figure 5c shows various photocurrent versus time traces measured with wavelengths in the range between 375 nm to 660 nm. At the beginning of the measurement the light is switched off and the current passing through the device has only the dark current contribution. When switching on the illumination (approximately at 5 seconds in the plot), the current passing through the device rapidly increases thanks to the additional contribution given by the photogenerated current. By extracting the height of the current step we can calculate the photocurrent and responsivity of our device. From the plot in Figure 5c one can see that the responsivity of the TiS_3 pristine device decreases when increasing the wavelength of the incident radiation. Figure 5d shows the photocurrent of the pristine device at 405 nm for different values of the illumination power density showing larger values for higher incident powers. Figure 5e-f shows similar measurements to those shown in Fig. 5c-d made on the oxidized nanoribbon photodetector. These measurements show that after oxidation the photocurrent decreases and the time response increases. Moreover, the photodetector responds only to light with wavelength shorter than 405 nm. The cut-off wavelength of the photodetector (defined as the largest wavelength for which the photodetector shows a response), is larger than 660 nm in the pristine case and blue-shifts to 405 nm in the oxidized state. As a control

Preprints (www.preprints.org) | NOT PEER-REVIEWED | Posted: 1 March 2020 doi:10.20944/preprints202003.0008.v1

Peer-reviewed version available at Nanomaterials 2020, 10, 711; doi:10.3390/nano10040711

fect of heat in absence of oxygen, see Section S2 of the Supporting Information. This device maintained the photodetecting properties of TiS_3 (responsivity spectrum and cut-off wavelength) even after 30 minutes at 320 °C.

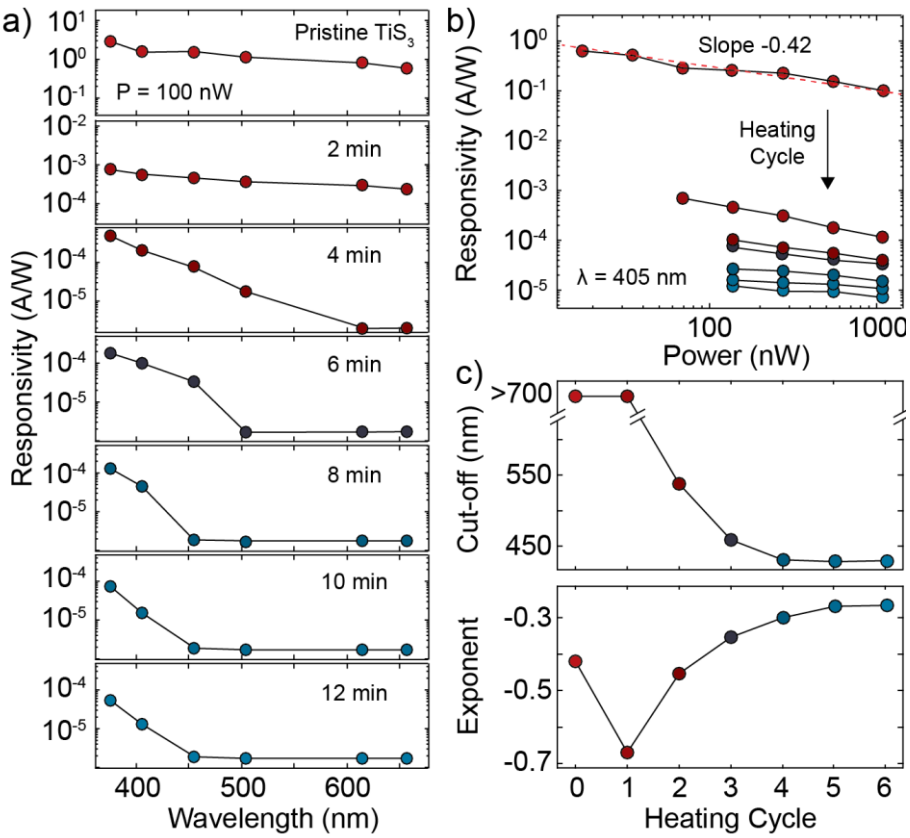

Figure 6: a) Responsivity of the device as a function of wavelength for different heating cycles. The pristine TiS_3 device (top) was heated at 320 °C in steps of 2 minutes and after each step the responsivity at different wavelengths was extracted. The three bottom curves correspond to the oxidized TiO_2 device. b) Responsivity of the device at 405 nm as a function of incident power for the pristine device (top curve) and after consecutive heating cycles. c) Responsivity cut-off wavelength (top) and responsivity-power exponent (bottom) as a function of heating cycle.

From current-time traces similar to the ones in Figure 5c-f we extracted the responsivity of the device, in its pristine state and after subsequent heating cycles, as a function of wavelength and incident power. Figure 6a shows the evolution of the wavelength-resolved responsivity of the device measured at an incident power of 100 nW during the heating process. The pristine device has a responsivity of approximately 1 A/W that after the first heating cycle decreases to 10^{-4} A/W. The dependence on the wavelength also gets modified by the heating process. While in the first three traces the device responds to all the probed wavelengths from 375 nm to 660 nm, in the last four traces the responsivity shows an abrupt decrease for wavelengths larger than 450 nm, indicating

that there is a blue shift of the cut-off wavelength of the photodetector. The wavelength resolved responsivity reported in the initial and final stages of the device are compatible with previously reported spectra of TiS_3 and TiO_2 photodetectors [17, 41].

Figure 6b shows the evolution of the responsivity at 405 nm as a function of the incident optical power. In a photodetector, the responsivity at a certain wavelength $R(\lambda)$ typically shows a power law dependence on the incident optical power P according to the formula:

$$R(\lambda) = P^{\alpha}$$

Where α is a dimensionless exponent, which is zero in the absence of traps and takes negative values when trap states participate in the generation of photocurrent [42-43]. The log-log plot shown in Figure 6b reveals that our device is characterized by a negative α for all the heating cycles since the slope of each curve in the figure gives directly the exponent α. Figure 6c shows the extracted cut-off wavelength and the exponent α of the device as a function of the heating cycle. The evolution of the cut-off wavelength is consistent with the predicted bandgap evolution shown in Figure 4a. As can be seen the exponent α starts from a value of -0.4 which indicates the presence of traps in the pristine TiS_3 device (0 heating cycle). After the first heating cycle the exponent decrease to a value of -0.7 indicating an increase in the density of the charge traps, which are probably due to the increase of defects by the reaction of sulfur (from TiS_3) with O_2 forming SO_2 as observed by TGA and MS (Figure 2b) and the presence of intercalated oxygen ($TiO_{2-x}S_x$) increasing the disorder (1-3 heating cycles). In the subsequent heating cycles (4-6) we observe a gradual increase of the value of the exponent α, sign of a reduction in the density of traps. The exponent α saturates around -0.25, a value larger than the starting value of -0.4, an indication that the final TiO_2 material contains less electronically active traps than the starting TiS_3 material. In TiS_3, sulfur vacancies are probably the dominant ones in trapping of the carriers [44-45].

Conclusions

In conclusion, we studied the thermal oxidation of TiS_3 nanoribbons with optical spectroscopy showing that this material can be converted to anatase TiO_2 in a controlled way. We built a photodetector based on a single TiS_3 nanoribbon and tuned its responsivity and cut-off wavelength by gradually oxidizing the nanoribbon. Ab-initio calculations of the band-structure of the materials are in agreement with the experiments. The shift of the cut-off wavelength in our photodetectors with a simple annealing step, demonstrates the ability to tune on demand the bandgap of the $TiO_{2-x}S_x$ for novel applications.

ACKNOWLEDGEMENTS

AC-G acknowledges funding from the European Commission under the Graphene Flagship, contract CNECTICT-604391. RF acknowledges support from the Netherlands Organisation for Scientific Research (NWO) through the research program Rubicon with project number 680-50-1515. RB

acknowledges funding from the European Union's Horizon 2020 research and innovation program under the Marie Skłodowska-Curie grant agreement No. 793318. RB and RDA acknowledge financial support by SElecT-DFT (Grant No. FIS2016-79464-P) of the Spanish Ministerio de Economia y Competitividad through the Agencia Estatal de Investigacion and the Fondo Europeo de Desarrollo Regional and Grupo Consolidado UPV/EHU del Gobierno Vasco (IT578-13). MIRE Group acknowledges funding from MINECO-FEDER through the project MAT2015-65203-R. KW and TT acknowledge the support of the Elemental Strategy Initiative conducted by the MEXT, Japan and the CREST (JPMJCR15F3), JST.

SUPPORTING INFORMATION

Additional optical characterization of TiS_3 and TiO_2 ribbons, TiS_3 photodetectors heated in vacuum, statistics of photodetectors studied in this work, stability of TiS_3 during Raman spectroscopy, additional details about theory.

COMPETING INTERESTS

The authors declare no competing financial interests.

REFERENCES

1. Schmidt, H.; Giustiniano, F.; Eda, G., Electronic transport properties of transition metal dichalcogenide field-effect devices: surface and interface effects. *Chem Soc Rev* **2015,** *44* (21), 7715-36.
2. Novoselov, K.; Mishchenko, A.; Carvalho, A.; Neto, A. C., 2D materials and van der Waals heterostructures. *Science* **2016,** *353* (6298), aac9439.
3. Frisenda, R.; Molina-Mendoza, A. J.; Mueller, T.; Castellanos-Gomez, A.; van der Zant, H. S., Atomically thin p–n junctions based on two-dimensional materials. *Chemical Society Reviews* **2018,** *47* (9), 3339-3358.
4. Chhowalla, M.; Shin, H. S.; Eda, G.; Li, L.-J.; Loh, K. P.; Zhang, H., The chemistry of two-dimensional layered transition metal dichalcogenide nanosheets. *Nature chemistry* **2013,** *5* (4), 263.
5. Favron, A.; Gaufres, E.; Fossard, F.; Phaneuf-L'Heureux, A. L.; Tang, N. Y.; Levesque, P. L.; Loiseau, A.; Leonelli, R.; Francoeur, S.; Martel, R., Photooxidation and quantum confinement effects in exfoliated black phosphorus. *Nat Mater* **2015,** *14* (8), 826-32.
6. Wang, G.; Pandey, R.; Karna, S. P., Physics and chemistry of oxidation of two-dimensional nanomaterials by molecular oxygen. *Wiley Interdisciplinary Reviews: Computational Molecular Science* **2017,** *7* (1), e1280.
7. Yang, S.; Jiang, C.; Wei, S.-h., Gas sensing in 2D materials. *Applied Physics Reviews* **2017,** *4* (2), 021304.
8. Li, Q.; Zhou, Q.; Shi, L.; Chen, Q.; Wang, J., Recent advances in oxidation and degradation mechanisms of ultrathin 2D materials under ambient conditions and their passivation strategies. *Journal of Materials Chemistry A* **2019,** *7* (9), 4291-4312.
9. Island, J. O.; Steele, G. A.; van der Zant, H. S.; Castellanos-Gomez, A., Environmental instability of few-layer black phosphorus. *2D Materials* **2015,** *2* (1), 011002.
10. Kuriakose, S.; Ahmed, T.; Balendhran, S.; Bansal, V.; Sriram, S.; Bhaskaran, M.; Walia, S., Black phosphorus: ambient degradation and strategies for protection. *2D Materials* **2018,** *5* (3), 032001.
11. Cartamil-Bueno, S. J.; Steeneken, P. G.; Tichelaar, F. D.; Navarro-Moratalla, E.; Venstra, W. J.; van Leeuwen, R.; Coronado, E.; van der Zant, H. S.; Steele, G. A.; Castellanos-Gomez, A., High-quality-factor tantalum oxide nanomechanical resonators by laser oxidation of TaSe 2. *Nano Research* **2015,** *8* (9), 2842-2849.
12. De Sanctis, A.; Amit, I.; Hepplestone, S. P.; Craciun, M. F.; Russo, S., Strain-engineered inverse charge-funnelling in layered semiconductors. *Nat Commun* **2018,** *9* (1), 1652.
13. Peimyoo, N.; Barnes, M. D.; Mehew, J. D.; De Sanctis, A.; Amit, I.; Escolar, J.; Anastasiou, K.; Rooney, A. P.; Haigh, S. J.; Russo, S.; Craciun, M. F.; Withers, F., Laser-writable high-k dielectric for van der Waals nanoelectronics. *Sci Adv* **2019,** *5* (1), eaau0906.
14. Nouchi, R.; Matsumoto, M.; Mitoma, N., Gate-controlled photo-oxidation of graphene for electronic structure modification. *Journal of Materials Chemistry C* **2019,** *7* (7), 1904-1912.
15. Island, J. O.; Barawi, M.; Biele, R.; Almazan, A.; Clamagirand, J. M.; Ares, J. R.; Sanchez, C.; van der Zant, H. S.; Alvarez, J. V.; D'Agosta, R.; Ferrer, I. J.; Castellanos-Gomez, A., TiS3 transistors with tailored morphology and electrical properties. *Advanced Materials* **2015,** *27* (16), 2595-601.
16. Island, J. O.; Biele, R.; Barawi, M.; Clamagirand, J. M.; Ares, J. R.; Sánchez, C.; van der Zant, H. S.; Ferrer, I. J.; D'Agosta, R.; Castellanos-Gomez, A., Titanium trisulfide (TiS3): a 2D semiconductor with quasi-1D optical and electronic properties. *Scientific Reports* **2016,** *6*, 22214.
17. Island, J. O.; Buscema, M.; Barawi, M.; Clamagirand, J. M.; Ares, J. R.; Sánchez, C.; Ferrer, I. J.; Steele, G. A.; van der Zant, H. S.; Castellanos-Gomez, A., Ultrahigh Photoresponse of Few-Layer TiS3 Nanoribbon Transistors. *Advanced Optical Materials* **2014,** *2* (7), 641-645.

effect transistors. *Nanoscale* **2015,** *7* (29), 12291-12296.
19. Molina-Mendoza, A. J.; Barawi, M.; Biele, R.; Flores, E.; Ares, J. R.; Sánchez, C.; Rubio-Bollinger, G.; Agraït, N.; D'Agosta, R.; Ferrer, I. J.; Castellanos-Gomez, A., Electronic Bandgap and Exciton Binding Energy of Layered Semiconductor TiS_3. *Advanced Electronic Materials* **2015,** *1* (9), 1500126.
20. Biele, R.; Flores, E.; Ares, J. R.; Sanchez, C.; Ferrer, I. J.; Rubio-Bollinger, G.; Castellanos-Gomez, A.; D'Agosta, R., Strain induced bang-gap engineering in layered TiS3. *Nano Research* **2015,** *11*, 225–232.
21. Dai, J.; Zeng, X. C., Titanium Trisulfide Monolayer: Theoretical Prediction of a New Direct-Gap Semiconductor with High and Anisotropic Carrier Mobility. *Angewandte Chemie* **2015,** *127* (26), 7682-7686.
22. Ferrer, I.; Ares, J.; Clamagirand, J.; Barawi, M.; Sánchez, C., Optical properties of titanium trisulphide (TiS 3) thin films. *Thin Solid Films* **2013,** *535*, 398-401.
23. Jin, Y.; Li, X.; Yang, J., Single layer of MX 3 (M= Ti, Zr; X= S, Se, Te): a new platform for nano-electronics and optics. *Physical Chemistry Chemical Physics* **2015,** *17* (28), 18665-18669.
24. Kang, J.; Sahin, H.; Ozaydin, H. D.; Senger, R. T.; Peeters, F. M., TiS3 nanoribbons: Width-independent band gap and strain-tunable electronic properties. *Physical Review B* **2015,** *92* (7), 075413.
25. Li, M.; Dai, J.; Zeng, X. C., Tuning the electronic properties of transition-metal trichalcogenides via tensile strain. *Nanoscale* **2015,** *7* (37), 15385-15391.
26. İyikanat, F.; Sahin, H.; Senger, R. T.; Peeters, F. M., Vacancy formation and oxidation characteristics of single layer TiS3. *J. Phys. Chem. C* **2015,** *119*, 10709-10715.
27. Miró, P.; Audiffred, M.; Heine, T., An atlas of two-dimensional materials. *Chemical Society Reviews* **2014,** *43* (18), 6537-6554.
28. Luttrell, T.; Halpegamage, S.; Tao, J.; Kramer, A.; Sutter, E.; Batzill, M., Why is anatase a better photocatalyst than rutile?-Model studies on epitaxial TiO 2 films. *Scientific reports* **2014,** *4*, 4043.
29. Mattsson, A.; Osterlund, L., Adsorption and photoinduced decomposition of acetone and acetic acid on anatase, brookite, and rutile TiO2 nanoparticles. *The Journal of Physical Chemistry C* **2010,** *114* (33), 14121-14132.
30. Flores, E.; Ares, J.; Ferrer, I.; Sánchez, C., Synthesis and characterization of a family of layered trichalcogenides for assisted hydrogen photogeneration. *physica status solidi (RRL)–Rapid Research Letters* **2016,** *10* (11), 802-806.
31. Molina-Mendoza, A. J.; Island, J. O.; Paz, W. S.; Clamagirand, J. M.; Ares, J. R.; Flores, E.; Leardini, F.; Sánchez, C.; Agraït, N.; Rubio-Bollinger, G., High Current Density Electrical Breakdown of TiS3 Nanoribbon-Based Field-Effect Transistors. *Advanced Functional Materials* **2017,** *27* (13), 1605647.
32. Frisenda, R.; Navarro-Moratalla, E.; Gant, P.; De Lara, D. P.; Jarillo-Herrero, P.; Gorbachev, R. V.; Castellanos-Gomez, A., Recent progress in the assembly of nanodevices and van der Waals heterostructures by deterministic placement of 2D materials. *Chemical Society Reviews* **2018,** *47*, 53-68.
33. Castellanos-Gomez, A.; Buscema, M.; Molenaar, R.; Singh, V.; Janssen, L.; van der Zant, H. S.; Steele, G. A., Deterministic transfer of two-dimensional materials by all-dry viscoelastic stamping. *2D Materials* **2014,** *1* (1), 011002.
34. Pawbake, A. S.; Island, J. O.; Flores, E.; Ares, J. R.; Sanchez, C.; Ferrer, I. J.; Jadkar, S. R.; van der Zant, H. S.; Castellanos-Gomez, A.; Late, D. J., Temperature-Dependent Raman Spectroscopy of Titanium Trisulfide (TiS_3) Nanoribbons and Nanosheets. *ACS Applied Materials & Interfaces* **2015,** *7* (43), 24185-90.
35. Ohsaka, T.; Izumi, F.; Fujiki, Y., Raman spectrum of anatase, TiO2. *Journal of Raman spectroscopy* **1978,** *7* (6), 321-324.
36. Zhang, Y.; Wu, W.; Zhang, K.; Liu, C.; Yu, A.; Peng, M.; Zhai, J., Raman study of 2D anatase TiO 2 nanosheets. *Physical Chemistry Chemical Physics* **2016,** *18* (47), 32178-32184.
37. Giannozzi, P.; Baroni, S.; Bonini, N.; Calandra, M.; Car, R.; Cavazzoni, C.; Ceresoli, D.; Chiarotti, G. L.; Cococcioni, M.; Dabo, I., QUANTUM ESPRESSO: a modular and open-source software project for quantum simulations of materials. *Journal of physics: Condensed matter* **2009,** *21* (39), 395502.
38. Hartwigsen, C.; Gœdecker, S.; Hutter, J., Relativistic separable dual-space Gaussian pseudopotentials from H to Rn. *Physical Review B* **1998,** *58* (7), 3641.
39. Goedecker, S.; Teter, M.; Hutter, J., Separable dual-space Gaussian pseudopotentials. *Physical Review B* **1996,** *54* (3), 1703.
40. Choudhary, K.; Kalish, I.; Beams, R.; Tavazza, F., High-throughput Identification and Characterization of Two-dimensional Materials using Density functional theory. *Scientific Reports* **2017,** *7* (1), 5179.
41. Molina-Mendoza, A.; Moya, A.; Frisenda, R.; Svatek, S. A.; Gant, P.; Gonzalez-Abad, S.; Antolín, E.; Agrait, N.; Bollinger, G. R.; de Lara, D. P., Highly responsive UV-photodetectors based on single electrospun TiO2 nanofibres. *Journal of Materials Chemistry C* **2016,** *4* (45), 10707-10714.
42. Soci, C.; Zhang, A.; Xiang, B.; Dayeh, S. A.; Aplin, D.; Park, J.; Bao, X.; Lo, Y.-H.; Wang, D., ZnO nanowire UV photodetectors with high internal gain. *Nano letters* **2007,** *7* (4), 1003-1009.
43. González-Posada, F.; Songmuang, R.; Den Hertog, M.; Monroy, E., Room-temperature photodetection dynamics of single GaN nanowires. *Nano letters* **2011,** *12* (1), 172-176.
44. Arsentev, M. Y.; Petrov, A.; Missyul, A.; Hammouri, M., Exfoliation, point defects and hydrogen storage properties of monolayer TiS 3: an ab initio study. *RSC Advances* **2018,** *8* (46), 26169-26179.
45. Furchi, M. M.; Polyushkin, D. K.; Pospischil, A.; Mueller, T., Mechanisms of photoconductivity in atomically thin MoS2. *Nano Lett* **2014,** *14* (11), 6165-70.

Preprints (www.preprints.org) | NOT PEER-REVIEWED | Posted: 1 March 2020 doi:10.20944/preprints202003.0008.v1

Peer-reviewed version available at *Nanomaterials* **2020**, *10*, 711; doi:10.3390/nano10040711

TOC graphic